5.1 Introduction

In photocatalysis reaction, photogenerated electrons and holes can initiate redox reactions at the surface of the semiconductor catalyst [128, 129]. Although, this photogenerated carrier generation by solar spectrum depends on the bandgap of the semiconductor. As a single semiconductor photocatalyst, TiO_2 has been used widely due to its high chemical stability [61], low toxicity [130], and its potential utility for the destruction of organic compounds in polluted air and waste water [131]. However, due to its large bandgap nature, it is capable of absorbing a very narrow region of the solar spectrum, which is capable of generating electron-hole pair at a very slow rate. To avoid this situation, photocatalyst with composite heterojunction semiconductor of low bandgap with the wide bandgap metal oxide has been investigated widely where photo generated electron can transfer to the conduction band of metal-oxide due to barrier potential [132]-[126]. In earlier reports, a number of metal chalcogenide nanoparticles (like Ag_2S [133], Cu_2S[111]) have been used as low bandgap components that absorb solar light mostly[134-136]. In a combination of these two issues, large and narrow bandgap heterojunction photocatalysis has emerged as a promising entrance to visible-near infrared (NIR) light-active photocatalysts for many applications, such as decomposition of organic pollutants, selective oxidation and reduction reactions of organic compounds and hydrogen generation from aqueous-alcoholic solutions [137-141]. However, photocatalytic proton reduction by the use of sacrificial reluctants like methanol, H_2 evolution rates of these heterojunction catalysts under visible light is still much lower. This lower performance occurs due to poor

heterostructure formation [67, 142]. Although These types of catalyst structures are quite effective, efficiency strongly depends on the nature of metal chalcogenide/metal-oxide interfaces [105, 143-145]. In most of those studies, metal chalcogenide NPs are deposited on top of TiO_2 surfaces that make poor interfaces with significant interface trap states. An ideal metal chalcogenide-metal oxide heterogeneous photocatalysis required a large interface with very low trap state to reach efficient charge transfer without significant recombination in interfacial trap state. Therefore, a better synthetic technique of metal chalcogenide-metal oxide composite is required to achieve higher interfaces with lower interface trap states to improve the catalytic performance.

In this study, a unique approach has been taken to develop *in situ* grown Ag_2S NPs within titanium oxide (TiO_2) thin film and has been utilized for photocatalytic H_2 generation. This thin film growth consists of three successive steps, including sol-gel derived ion-conducting thin film fabrication containing loosely bound light ion (Li^+) followed by ion-exchange (with Ag^+) and subsequent sulfurization process. In this process, large area Ag_2S-TiO_2 thin film containing Ag_2S NPs with size ranging ~10-70 nm was readily obtained. The Ag_2S-NPs size and interparticle distance were controlled by changing the growth conditions. The photo-electrocatalytic performance of Ag_2S-TiO_2 composite thin films was evaluated by photo-electrochemical water splitting for the evolution of hydrogen, as discussed in subsequent sections. A transfer-enhancement synergistic mechanism has been proposed to explain the experimental results.

5.2 Results and Discussions

5.2.1 Structural and optical characterization

The X-ray diffraction (XRD) patterns of the samples were collected at room temperature. **Figures 5.1(a)** shows the x-ray diffraction (XRD) pattern of $Li_4Ti_5O_{12}$ (LTO),

TiO_2, and Ag_2S-TiO_2 dip-coated thin films that have been deposited on FTO substrate. The diffraction peaks of LTO are located at 2θ ~ 18.5, 35.6, 43.7, corresponding reflection planes (111), (311), and (331), respectively, that have been well matching with JCPDS file no. 490207, confirmed the cubic spinel structure with the space group of (F $\bar{3}$dm). Similarly, the diffraction peaks of TiO_2 are 25.36°, 37.88°, 48.11° and 54.12° corresponding to the planes (101), (004), (200) and (105) respectively, nicely matched with JCPDS card No. 894921, indicates the tetragonal structure with the space group of ($I4_1$).

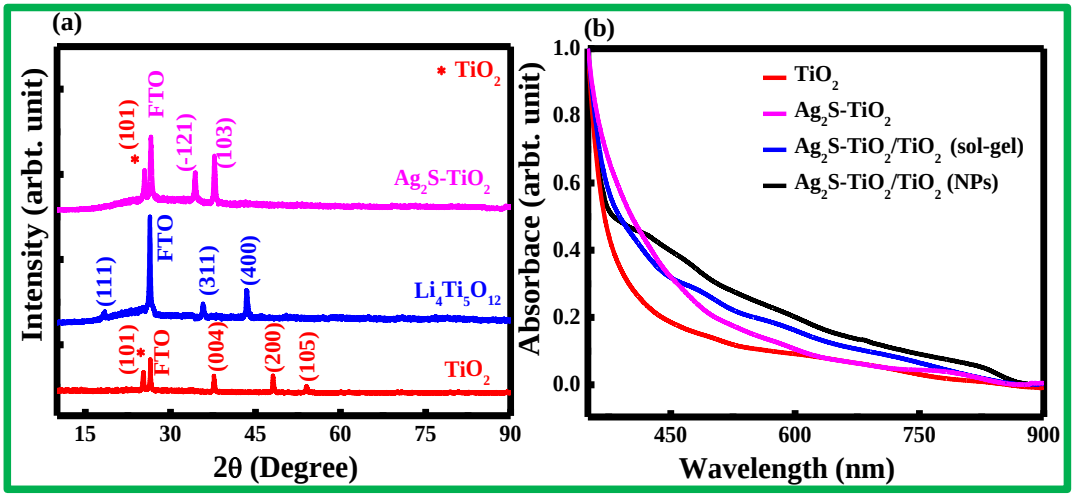

***Figure 5.1**: (a) The XRD pattern of bare TiO_2, LTO and Ag_2S-TiO_2 thin films (b) Normalized UV-VIS absorption spectra of TiO_2 and Ag_2S-TiO_2nanocomposite thin films.*

The diffraction peaks of Ag_2S-TiO_2 thin film that has been shown in **figure 5.1(a)** indicates the peak positions of 2θ ~34.42° and 37.10° and the corresponding diffraction planes are (-121), (013), match with JCPDF card number 140072. It is known that TiO_2 has three different crystallographic phases of (a) rutile (a) anatase and (c) brookite, and among these phases, anatase is thermodynamically more stable than rutile and brookite [121, 135, 146]. This XRD study of Ag_2S-TiO_2 thin film has identified the formation of anatase phase that has a peak position at 2θ ~25.35° and 54. 35° correspond to the planes (101) and (105)

[121]. **Figure 5.1(b)** shows the normalized UV-VIS absorption spectra of different photoanodes coated with TiO_2 (sol-gel), Ag_2S-TiO_2/TiO_2 (sol-gel), and Ag_2S-TiO_2/TiO_2 NPs thin film within the wavelength range of 300-900 nm. Absorption spectra of TiO_2 (sol-gel) thin-film show strong absorption in the UV region (300 nm) only with a steadily lower absorption in higher wavelength light,

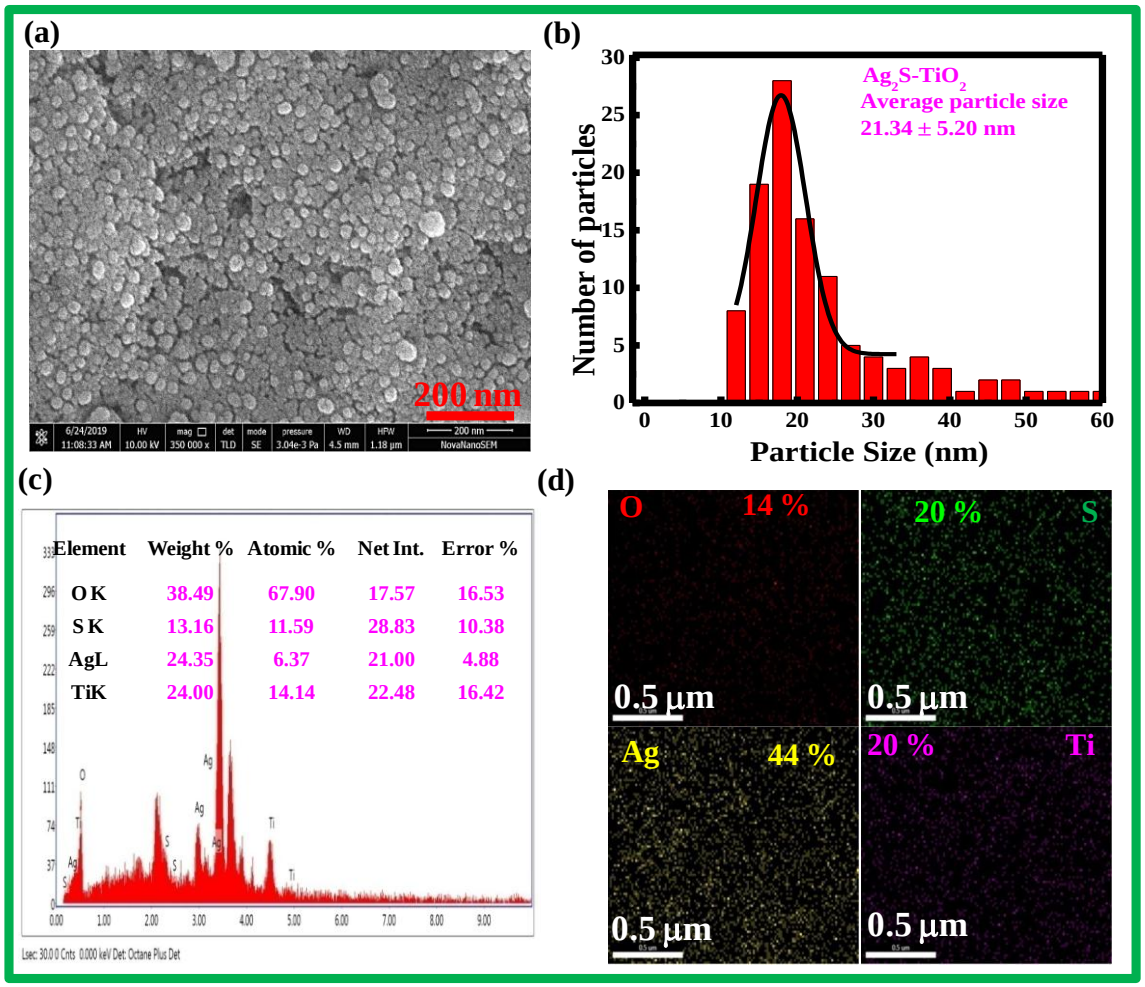

Figure 5.2 *The surface morphology of the (a)* Ag_2S-TiO_2 (dip coated) thin film *on FTO coated glass substrate (b) Particle size distribution of* Ag_2S-TiO_2 *NPs (c) Energy dispersive spectra of* Ag_2S-TiO_2 *thin film, an elemental composition that obtained from EDS is shown in the inset. (d) EDS mapping of* Ag_2S-TiO_2 *thin film (i) O (ii) for S, (iii) for Ag, and(iv) for Ti.*

which is expected the result for TiO_2 (bandgap ~3.2 eV) thin film. On the other hand, Ag_2S-TiO_2 coated thin film shows a significant enhancement of absorption in the visible

region due to the formation of narrow bandgap Ag_2S nanocrystal inside the TiO_2 thin film. Such kind of enhanced absorption has been observed in earlier reports on Ag_2S-TiO_2 thin film [147, 148].

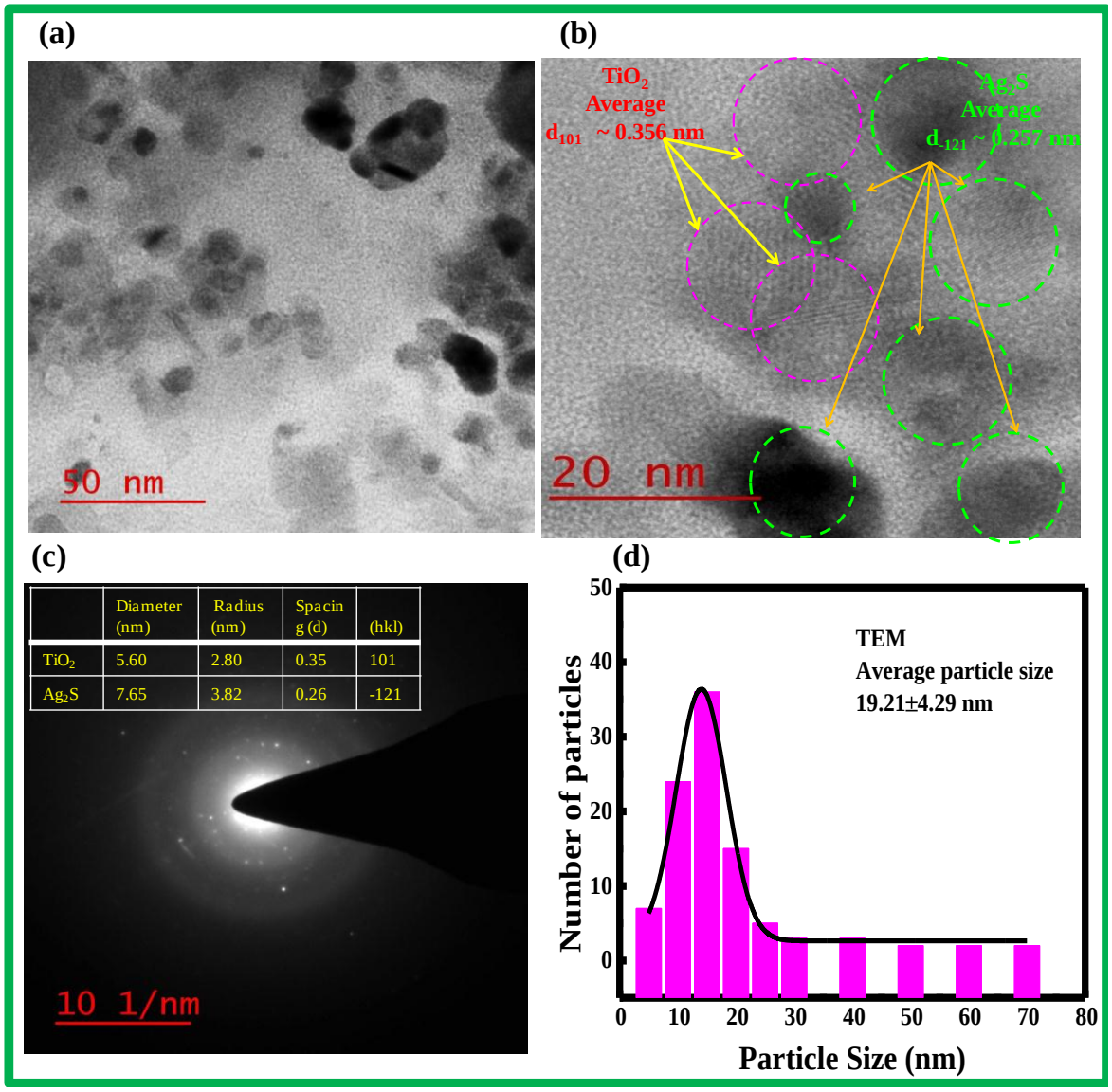

Figure 5.3*(a) Transmission electron microscope image of Ag_2S NP-TiO_2 (b) high resolution image of Ag_2S NP-TiO_2, green circle indicates the lattice d-fringe of Ag_2S and pinck circle for TiO_2.(c) Slected area diffraction pattern of Ag_2S NPs-TiO_2 (d) Size distrbution of Ag_2S NPs-TiO_2.*

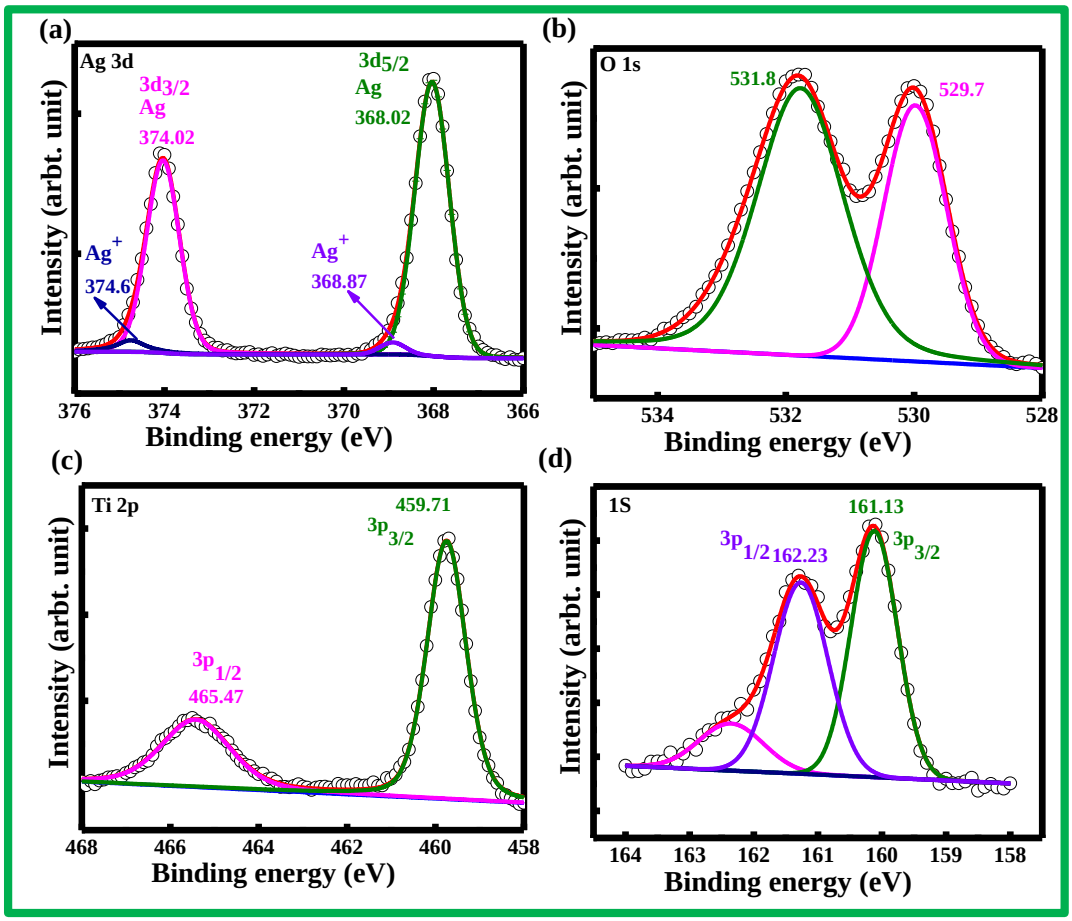

***Figure 5.4**:High-resolution XPS spectra of Ag_2S-TiO_2 sample (a) Ag 3d (b) O 1s. (c) Ti 2p and (d) S 3p*

5.2.2 Surface morphology and microstructral characterization

The surface morphology and size of Ag_2S nanoparticle were investigated by scanning electron microscopy (SEM), which shown in **figure 5.2(a)**. For SEM analysis, the **s**amples were prepared on a glass substrate by the dip-coating method. Similar dip-coating samples were prepared with a 300 mM precursor solution of LTO with a dipping speed of 2 mm/s followed by an annealing process. After that, all these substrates were gone through the ion-exchange process and subsequent sulfurization process to grow Ag_2S NPs-TiO_2 thin film. **Figure 5.2(a)** shows the Ag_2S-TiO_2 film that was prepared by a dip-coating method with a concentration of 300 mM which indicates the Ag_2S nanocrystal formation

inside the TiO_2 matrix. Additionally, it gives information about the size of Ag_2S NP are spherical with an average particle size of 21 nm and uniformly distributed shown in the **figure 5.2(b).** The composition and content of the metallic element of the Ag_2S-TiO_2 samples were determined by an energy-dispersive X-ray spectrometer (EDX) attached to the HR-SEM (**in figure 5.2(c)).** This picture clearly shows the existence of Ag, S, Ti and O elements inside thin film. Elemental mapping is carried out by using Energy Dispersive X-ray Spectrometry (EDS), which shown in **figure 5.2(d).** A uniform distribution of Ti, Ag, and S through the film indicates the uniform growth of Ag_2S NP in the $TiO_2$the film.

For more detail structural analysis, a transmission electron microscopy (TEM) study has been done which shown in **figure 5.3**. For sample preparation of this study, Ag_2S-TiO_2 thin film was scratched from the substrate and made a fine powder by using a grinding mortar that was dispersed in chloroform by keeping the solution in an ultrasonic bath for 1 hour. **Figure 5.3(a)** shows thelower magnification of TEM image, which indicated Ag_2S-NPs formation in the TiO_2 matrix. This picture also shows that the particle size is distributed mostly within the range of 10-70 nm with an average particle size of 19 nm. Particle size distribution has been shown in the **figure 5.3(b)**. This distribution is very much similar to SEM analysis. High-resolution image (**Figure 5.3(c)** of Ag_2S NP-TiO_2 shows the lattice fringe formation of Ag_2S-NPs and TiO_2 individually and their co-existence. The average value of d spacing for Ag_2S-NPs and TiO_2 are 0.26 and 0.35 nm, respectively, that are corresponding to Ag_2S (-121) and anatase TiO_2(101) planes and d spacing also match with selected area diffraction pattern (SAD) shown in the **figure 5.3 (d)**. The XRD analysis of the Ag_2S-TiO_2 sample (**Figure 5.1(a)**), these two respective planes of Ag_2S and TiO_2 have been seen clearly.

5.2.3 X-ray photoemission spectroscopy (XPS)

X-ray photoemission spectroscopy (XPS) study was carried out to investigate the chemical oxidation state of the elements presented in the nanocomposite Ag_2S-TiO_2 thin film. The XPS spectra of Ag 3d, O 1s, Ti 2p, and S 3p are detected in the Ag_2S-TiO_2 system and shown in figure 5.4. **Figure 5.4(a)** shows that the Ag 3d has two intense peaks at 374.02 and 368.02 eV, which corresponds to the binding energy of Ag $3d_{3/2}$ and Ag $3d_{5/2}$ respectively, Two peaks (**Figure. 5.4(b)** appear for O 1s at the binding energies of 531.81eV, 529.71 eV which correspond to O in TiO_2 and oxygen vacancies respectively, two peaks appear with intensities of Ti $2p_{1/2}$ and Ti $2p_{3/2}$ at 465.47 eV, and 459.71 eV which are characteristic for Ti^{+4} are shown in figure 4c, this is attributed that to the Ti-O-Ti bond. Which supporting the presence of TiO_2 [149]. Two peaks appear with intensities of S $3p_{1/2}$and S $3p_{3/2}$ at 162.23 eV and 160.13 eV, which are characteristic for S^{2-} are shown in **figure 5.4(d)**.These peaks are supporting the presence of Ag and S in the Ag_2S system [150]. All these peak positions are well-matched with earlier reported of Ag_2S-TiO_2 systems [135, 151]. Therefore, the XPS study of this sample gives another proof of the formation of Ag_2S-TiO_2 film.

5.2.4 Photoelectro-chemical H_2 generation study

Figure 5.5(a) shows the photoelectrochemical properties for three different Ag_2S-TiO_2coated photoanodes that are grown on three different substrates, including FTO, TiO_2 (sol-gel)/FTO and TiO_2-NPs/FTO thin films, in 1 M KOH solution under white light (100 mW/m^2) and dark conditions. As it is shown in this **figure 5.5(a)**, for all three different types of Ag_2S-TiO_2 photoanodes, there is around one order difference of current between

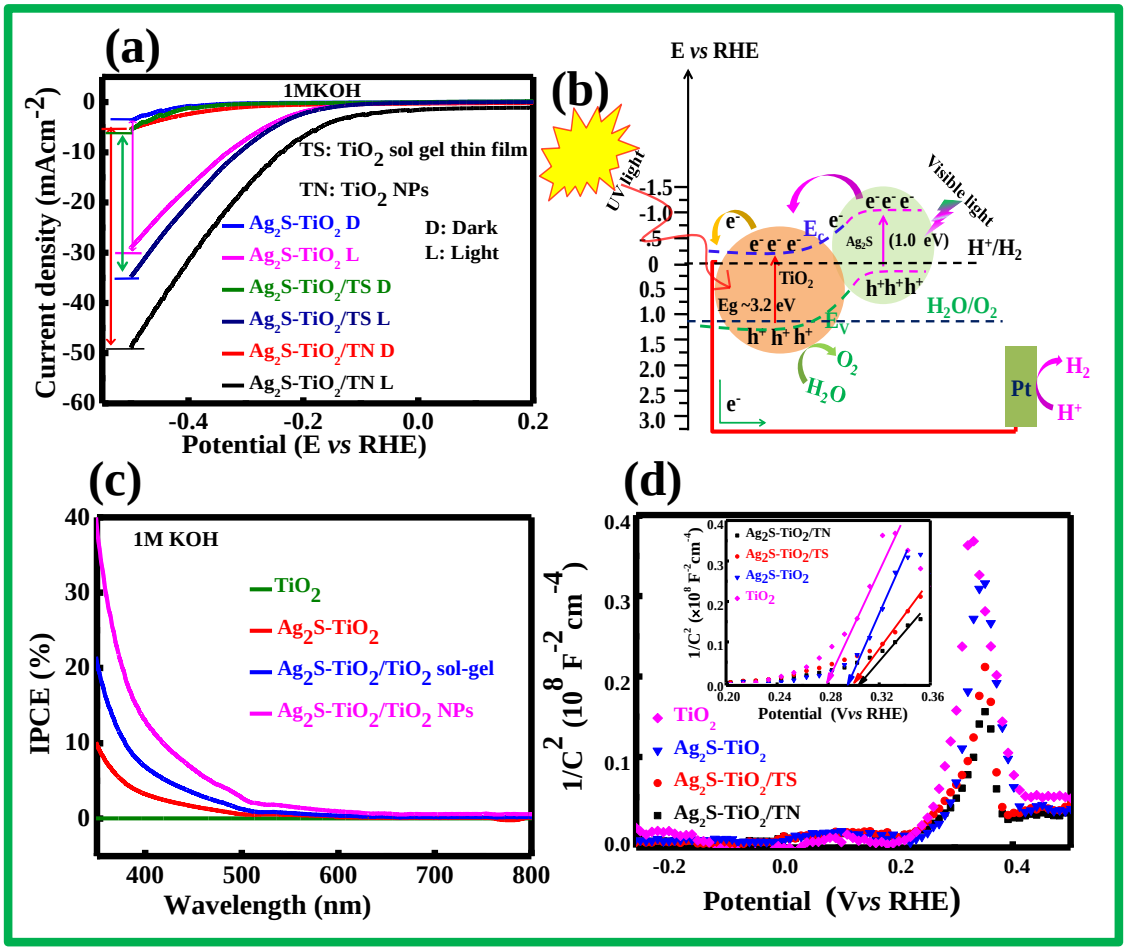

Figure 5.5 *(a) Current density vs. (V vs. RHE) potential of different Ag_2S-TiO_2 thin film under light and dark in 1 M KOH solution (b) schematic diagram of photocatalytic water splitting mechanism by Ag_2S-TiO_2 based photoanode (c) IPCE data for different photoanode in the range of 350 nm to 800 nm under -1.0V external bias with 1 M KOH electrolyte solution. (d) The Mott−Schottky (M-S) plot for different photoanodes in 1 kHz operation under dark condition.*

light and dark conditions. Again, the photocurrent of Ag_2S-TiO_2photoanode increases considerably in addition to underlying TiO_2 thin film. Highest photocurrent was observed of Ag_2S-TiO_2 photoanode with TiO_2 NPs with a current density of 49 $mA.cm^{-2}$ at -0.5 V external bias whereas photocurrent for Ag_2S-TiO_2/FTO, Ag_2S-TiO_2/TiO_2 (sol-gel)/FTO under same conditions are 35 and 29 $mAcm^{-2}$ respectively. To the best of our knowledge, these current densities are significantly higher with respect to earlier publications on Ag_2S-

TiO_2 photoanode systems [71, 146, 147, 152]. Again, this current density is ~5000 times higher compared to the only TiO_2 coated photoanode (0.01 $mAcm^{-2}$) under the same visible light illumination (in the figure 5.6(a)). This enhancement of photocurrent density has been occurred due to two different reasons. One of them is due to the larger amount of solar light absorption by low band Ag_2S NPs (0.9-1.1 eV), resulting there is of a large enhancement of photogenerated electron-hole generation. The other reason is the fast charge transfer of the photogenerated electrons from electronically coupled Ag_2S NPs to TiO_2, resulting in a significant reduction of the electron-hole recombination. This phenomenon has been schematically presented in **figure 5.5(b)**.This picture indicates that as soon, visible light is illuminated on Ag_2S-TiO_2 photoanodes, major part of that spectrum is absorbed by lower bandgap Ag_2S NPs and generates electron-hole pair. This photogenerated electron of Ag_2S NPs is then transferred to the CB of TiO_2. This charge transfer process of electronically coupled Ag_2S/TiO_2 heterojunction is energetically favorable because of the existence of CB of Ag_2S above that of TiO_2. Of course, a small fraction of solar spectrum that lies in UV region is absorbed by TiO_2 and generates electron-hole pair. The photogenerated electron of Ag_2S-TiO_2 thin film is then transferred from CB of TiO_2 to FTO electrode from where it reaches the Pt cathode where it generates H_2. Similarly, photogenerated hole of TiO_2 is added with the photogenerated hole of Ag_2S NP due to the existence of VB of Ag_2S NP above the VB of TiO_2. These photogenerated holes of Ag_2S NPs are then reacted with electrolyte solution, which produced OH and H^+ that has been described by equations (5.7) and (5.8). These h^+ ions then reach to Pt cathode where it accepts one electron to form H_2. This complete photoelectrochemical process has been shown in equations (5.1) to (5.8). As observed in our photoelectrochemical study, these charge transfer processes can be

enhanced by adding additional TiO_2 thin film that can be fabricated either by sol-gel or by NPs solution that results in higher photocurrent generation that as grown Ag_2S-TiO_2 thin film.

In electrolyte

$$H_2O \longrightarrow OH^- + H^+ \quad (5.1)$$

At anode

$$TiO_2 + hv\ (UV\ light) \longrightarrow CB_{TiO_2}(e^-) + VB_{TiO_2}(h^+) \quad (5.2)$$

$$Ag_2S + hv\ (visible\ light) \longrightarrow CB_{Ag_2S}(e^-) + VB_{Ag_2S}(h^+) \quad (5.3)$$

$$CB_{Ag_2S}(e^-) + CB_{TiO_2} \longrightarrow VB_{Ag_2S}(h^+) + CB_{TiO_2}(e^-) \quad (5.4)$$

$$CB_{Ag_2S}(e^-) + CB_{TiO_2}(e^-) \longrightarrow VB_{Ag_2S}(h^+, h^+) + CB_{TiO_2}(e^-, e^-) \quad (5.5)$$

$$VB_{Ag_2S}(h^+) + OH^- \longrightarrow OH + H^+ \quad (5.6)$$

$$4OH \longrightarrow 2H_2O + O_2 \quad (5.7)$$

At counter electrode

$$2H^+ + 2e^- \longrightarrow H_2 \quad (5.8)$$

5.2.5 IPCE Measurements

The photocurrent generation rate in different spectral ranges has been studied by measuring IPCE data of different photoanodes. A comparative IPCE data of different Ag_2S-TiO_2 photoanode under -1.0 V external bias has been shown in **figure 5.5 (c)**. In addition, IPCE data of a TiO_2 (sol-gel) coated photoanode has been added as a reference to this study. As it is shown in **figure 5.5(c)**, the IPCE spectrum of all Ag_2S-TiO_2photoanode is very much similar with a very strong photocurrent generation in the region 350-500 nm thin film (Figure-2b). Compare to the data, TiO_2 (sol-gel) photoanode contributes a very week photocurrent that generated bellow 400 nm wavelength, which is due to the wide bandgap nature of TiO_2. These features of IPCE data indicated that the major part of photocurrent associated with H_2 generation is originated from the Ag_2S NPs. Comparative IPCE study of

different Ag_2S-TiO_2photoanodes shows that the highest value of IPCE has been achieved for the Ag_2S-TiO_2 /TiO_2 NPs/FTO sample with a value of ~ 12.5 % at 400 nm. This study implies that additional TiO_2 layer enhanced the charge transfer rate to the FTO electrode. On comparing TiO_2-NPs and TiO_2 -sol-gel thin film, the earlier one shows higher level photocurrent generation, is mostly due to the more compact TiO_2 thin film that forms relatively fewer trap states.

5.2.6 AC impedance study and Mott−Schottky (M-S) Measurements

Mott−Schottky (M-S) measurements were carried out for a better understanding of the hot-electron transport properties in photoanodes, which is shown in **figure 5.5(d)**. This experiment has been performed on different photoanodes coated with pure TiO_2 (sol-gel), Ag_2S-TiO_2, Ag_2S-TiO_2/TiO_2 sol-gel, and Ag_2S-TiO_2/TiO_2 NPs at an applied frequency of 1 kHz under dark conditions. The flat band potential (E_{FD}) of the semiconductor-electrolyte interface and the surface charge density (N_D) values were calculated by using the Mott−Schottky [75, 76] equation (5.9).

$$\frac{1}{C^2} = \frac{2}{e\,\varepsilon_0\,\varepsilon_r N_D}\left(E_{app} - E_{FD} - \frac{kT}{e}\right) \qquad (5.9)$$

Where C is the interfacial capacitance, E_{FD} is the flat band potential, k (1.3807×10^{-23}) is the Boltzmann constant; e is the electronic charge (1.6×10^{-19} coulomb), and T is the temperature of the system (~300K). The Mott−Schottky plot for different photoanodes shows a linear variation of $1/C^2$ with the applied potential. The M-S plot of all photoanodes shows positive slopes which indicate the n-type semiconductor nature of photoanodes. The flat E_{FD} of the photoanode was determined from the intersection of the slope with the x-axis of the plot. A positive shift of E_{FD} has been observed in all Ag_2S-TiO_2photoanodes

with respect to the reference TiO_2photoanode, which implies a significant enhancement of charge transfer rate due to the formation of Ag_2S. The highest value of E_{FD} has been observed for Ag_2S-TiO_2/TiO_2 NPs coated photoanode, which implies the most efficient charge transfer rate among four different photoanodes. The surface charge density(N_D) has been calculated by using the slop of M-S plot which is related by following equation[75, 76] (5.10).

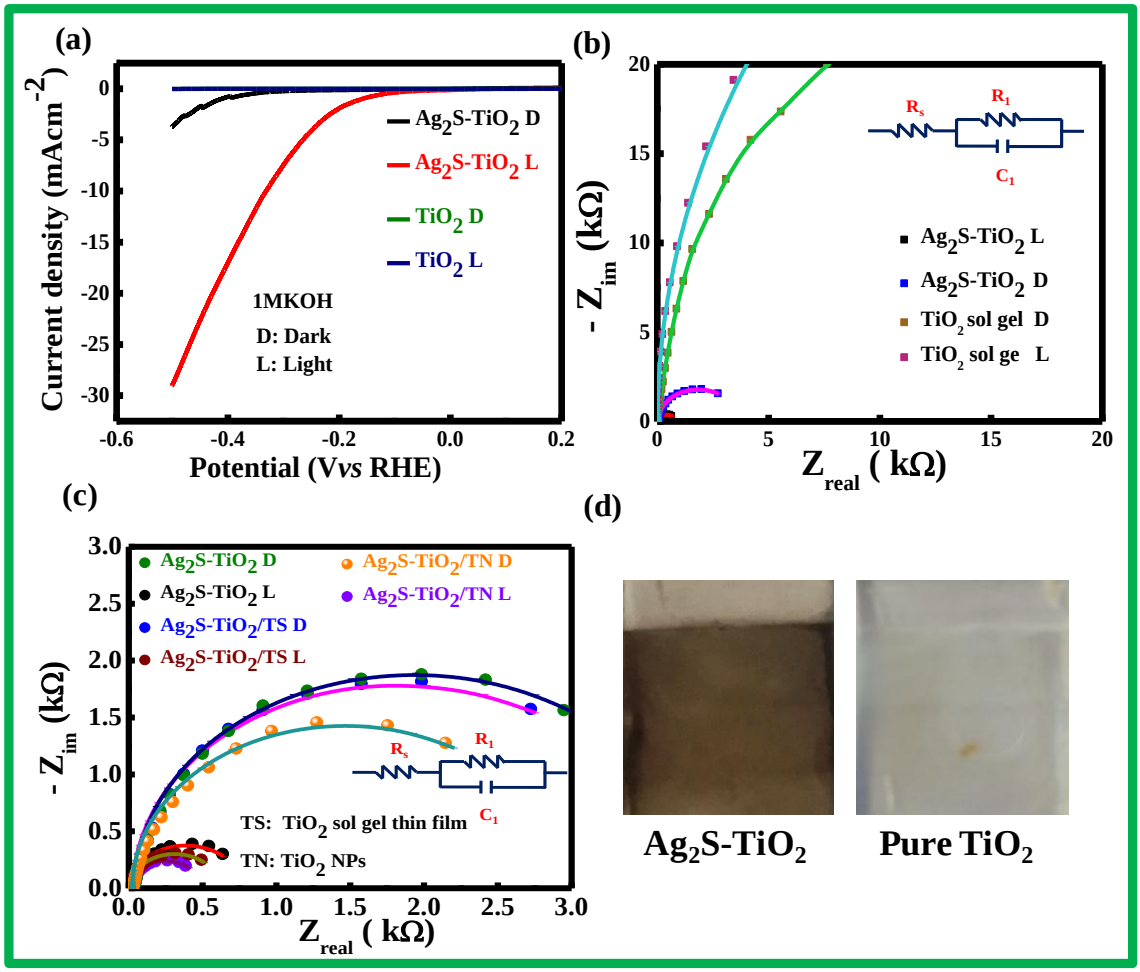

Figure 5.6:*(a) The comparative study of current density vs. (V vs. RHE) potential of bare TiO_2 and Ag_2S-TiO_2 thin film (b) The EIS spectra TiO_2 and Ag_2S TiO_2 photoanodes. The inset shows the equivalent circuit, (c) The electrochemical impedance spectroscopy (EIS) measurement for three different Ag_2S-TiO_2photoanodes under light and dark conditions in1 M KOH solution (d) The images of the Ag_2S-TiO_2 and TiO_2 (NP) photoanodes.*

$$N_D = \frac{2}{e\varepsilon_0\,\varepsilon_r}\frac{dE}{d(\frac{1}{C^2})} \qquad (5.10)$$

It is observed that the extracted values of N_D are largely enhanced due to the Ag_2S-TiO_2 thin film formation with respect to TiO_2 (only) thin film. The highest value of N_D has been determined for Ag_2S-TiO_2/TiO_2 NPs thin film, which is responsible for the reduction in the ohmic resistance of the film that leads to improving the higher rate charge transfer from photoanode to the FTO electrode.

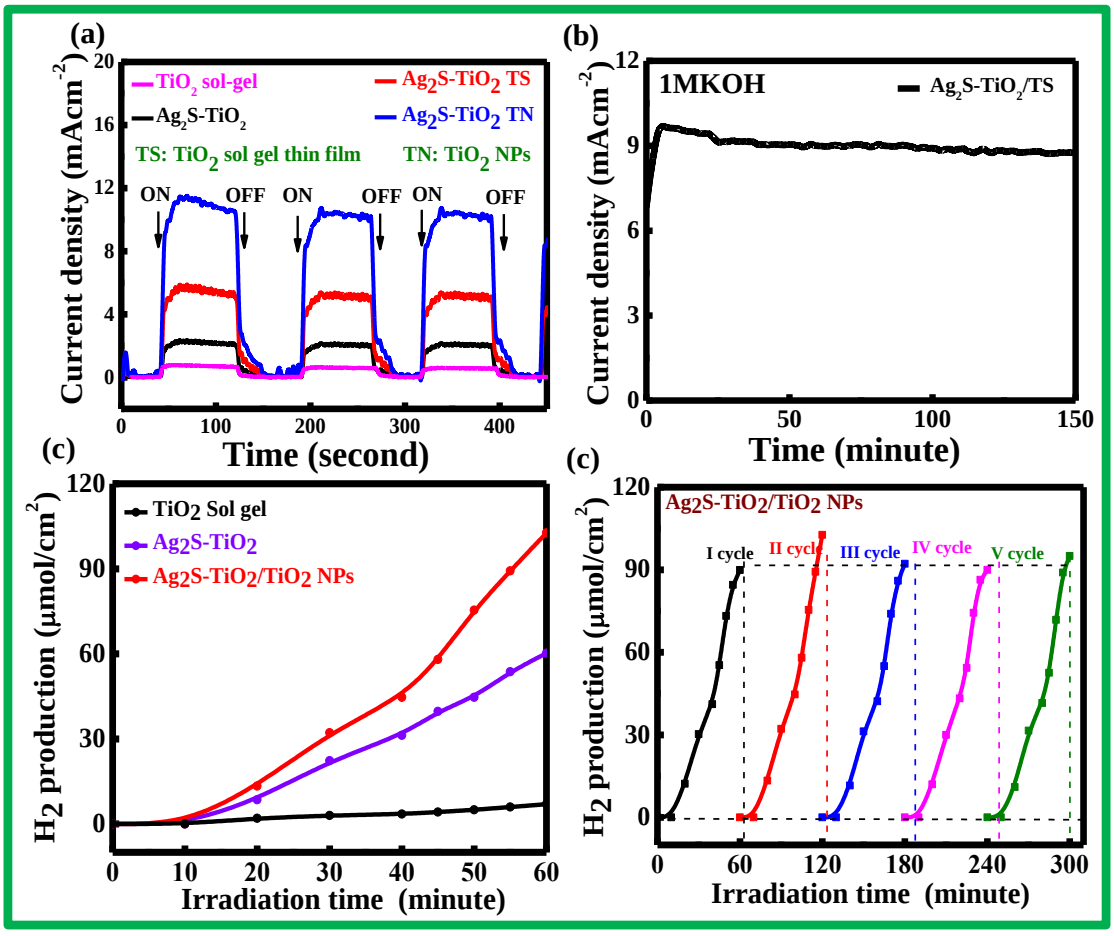

Figure 5.7: *(a) Time response of same photoanode with different substrates (b) Photostability tested for Ag_2S-TiO_2/TiO_2 sol-gel/FTO photoanode under light (100 mW/cm^2) with -0.5 V external bias in 1M KOH medium, The volumetric hydrogen generation under one sun white light irradiation with the time (c) for three different photoanodes. (d) In five successive cycles by Ag_2S-TiO_2/TiO_2 NP photoanode.*

The summary of E_{FD} and N_D values for all of these photoanodes are summarized in the table 5.1.

Table 5.1: The summary of the flat band potential and surface charge density (N_D) at 1kHz for the different devices.

Device structure	Slope from M-S curve at 1KHz	Flat Band potential (V)	N_D (cm^{-3})
Pure TiO_2	9.20×10^8	0.280	1.53×10^{19}
Ag_2S-TiO_2	6.48×10^8	0.290	2.17×10^{19}
Ag_2S-TiO_2/ TiO_2 sol-gel	4.06×10^8	0.296	3.47×10^{19}
Ag_2S-TiO_2/ TiO_2 NPs	2.62×10^8	0.301	5.38×10^{19}

Figure 5.6(b-c) shows the electrochemical impedance spectroscopy (EIS) measurement for three different Ag_2S-TiO_2photoanodes under light and dark conditions. As observed, there is a big difference of EIS data under dark and light for all these photoanodes, indicating that there is a large variation of resistances under these two conditions. The comparative EIS study shows that the semicircles of Ag_2S-TiO_2/TiO_2 NP/FTO are smaller than two other photoanodes both under dark and light conditions, which indicates the resistance of this sample is least than two others. Moreover, the smaller semicircle suggests that the charge transfer rate and separation rate of photogenerated electron-hole are higher compare to other samples. Inset shows the equivalent circuit of photoelectrochemical measurement set-up that includes the solution resistance (R_S) in series with the parallel connection of interfacial charge-transfer resistance of the photoanode/electrolyte interface (R_1) and double-layer capacitance (C_1) associated with the charge transfer process. All EIS data are

fitted according to this equivalent circuit. Summary of R_1 for all three Ag_2S-TiO_2photoanode under light and dark conditions are given in the table 5.2. The comparative EIS study between different Ag_2S-TiO_2photoanodes is shown in **figure 5.6(c).**

Table 5.2: Fitting value of R_s and R_1 for bare TiO_2 and Ag_2S-TiO_2 for all different photo-anodes under dark and light conditions.

Device structure	Rs (kΩ)		R_1 (kΩ)	
	under dark	under light	under dark	under light
Pure TiO_2	0.040	0.012	40.24	21.02
Ag_2S-TiO_2	0.030	0.009	3.80	0.756
Ag_2S-TiO_2/ TiO_2 sol-gel	0.024	0.007	3.50	0.605
Ag_2S-TiO_2/ TiO_2 NPs	0.025	0.007	2.80	0.484

Table 5.3 Summary of rising and falling time of different photoanodes.

Device structure	Raising time (Second)	Falling time (Second)
Pure TiO_2	3.82	6.85
Ag_2S-TiO_2	3.61	6.51
Ag_2S-TiO_2/ TiO_2 sol-gel	3.41	5.42
Ag_2S-TiO_2/ TiO_2 NPs	3.40	5.34

This shows that the formation of Ag_2S NPs inside TiO_2 thin film reduces the resistance of the photoanode both under dark and light conditions. The image of the samples shown in the **figure 5.6(d)**.

5.2.7 Volumetric hydrogen generation rate and time response Measurements

Time response of different photoanodes under light (100 mW/cm^2) and dark with -0.5 V external bias has been shown in **figure 5.7(b)** for Ag_2S-TiO_2 that indicates that the

photoresponse is repeatable. Rise time and fall time of Ag_2S-TiO_2/TiO_2 (NPs)/FTO are 3.4S and 5.3S respectively that implies that fast response of these photoanodes.Summary of rising time and fall time of all samples are summarized in table 5.3. The stability of Ag_2S-TiO_2 photoanode with TiO_2 sol-gel thin film was carried out in 1 M KOH for around 200 minutes under white light illumination, which shows the initial growth of photocurrent and then becomes stable over time. This study implies the good stability of these Ag_2S-TiO_2 thin films **(Figure 5.7(a))**.

The volumetric hydrogen generation over 60 minutes has observed by continuous irradiation by the white light of one sun and by collecting generated hydrogen, which shown in figure-5.7(c). This experiment has been performed for Ag_2S-TiO_2 thin film with and without TiO_2 NPs under laying photoanode. In addition, the TiO_2 (sol-gel) photoanode has been tested for references. As it showed from **figure 5.7(c)**, the higher rate of H_2 has been generated by Ag_2S-TiO_2/TiO_2 (NPs)/FTO photoanode with a production rate of ~ 90 $\mu mol/cm^2$ which isalmost ~1.5 times higher than Ag_2S-TiO_2/FTO photoanode and 20 times of TiO_2/FTO photoanode. This H_2 generation experiment has been performed in five successive cycles with Ag_2S-TiO_2 /TiO_2 NPs/FTO photoanode, which shown in **figure 5.7(d)**. As observed, this production rate is very much similar in all five different cycles.

5.3 Conclusions

In summary, large area Ag_2S–TiO_2 thin film has been fabricated in a simple solution-based technique. This growth technique requires three successive steps that include the fabrication of $Li_4Ti_5O_{12}$ ceramic thin film by sol-gel technique followed by an ion-exchange process that replaces Li^+ by Ag^+ to form $Ag_4Ti_5O_{12}$ thin film. Finally, $Ag_4Ti_5O_{12}$ thin-film converted to Ag_2S -TiO_2 due to the conversion of Ag^+ to Ag_2S. Such kind of *in*

situ growth of Ag_2S NP inside TiO_2 allows forming a large interface area of Ag_2S /TiO_2 composite with a lesser interface trap state. Formation of Ag_2S-TiO_2 was confirmed by SEM, XRD, XPS and UV-VIS absorption study. Photoelectrochemical measurements were carried out of this Ag_2S-TiO_2 thin film photoanodes to identify its applicability for H_2 generation. For this study, Ag_2S-TiO_2 thin films are grown on three different substrates including FTO, TiO_2 sol-gel/FTO, and TiO_2 NP/FTO coated glass and the comparative photo-electrocatalytic measurement of these photoanodes showed that sample onTiO_2 NP/FTO substrate generates the highest photocurrent of density 50 mA cm^{-2}at 0.5 V vs NHE in 1M KOH solution which is ~5000 times higher than pure TiO_2photoanode. Volumetric measurement shows that this generation rate is ~ 90 μmol/cm^2/hour. This current density is significantly higher than earlier reported Ag_2S/TiO_2 system. Moreover, this photocurrent shows good stability that has been tested for more than 1.5 hours. In futuristic, the present process can be extended for the fabrication of other metal chalcogenides-metal oxide composite systems for energy-related applications.